Surface & Coatings Technology 513 (2025) 132466

Contents lists available at ScienceDirect

Surface & Coatings Technology

journal homepage: www.elsevier.com/locate/surfcoat

Enhancement of wear resistance in AZ31 alloy by laser melt injection of high-volume-fraction titanium carbide particles

Zhenzhen Gui [a,*], Pengxi Liu [a], Keying Zhu [a], Yuanyuan Lu [b,*], Chaowen Guo [a], Tao Zou [a], Liu Cao [a], Fan Zhang [a,*], Tao Zhang [c,*], Dejian Liu [d]

[a] School of Mechanical and Electrical Engineering, Guangzhou University, 230 Wai Huan Xi Road, Guangzhou Higher Education Mega Center, Guangzhou 510006, China
[b] Engineering and Technology College, Hubei University of Technology, Wuhan 430068, China
[c] School of Physical and Materials Science, Guangzhou University, 230 Wai Huan Xi Road, Guangzhou Higher Education Mega Center, Guangzhou 510006, China
[d] State Key Laboratory of Materials Processing and Die & Mould Technology, Huazhong University of Science and Technology, Wuhan 430074, China

ARTICLE INFO

Keywords:
Laser melt injection
Rapid solidification
Ceramic particle reinforcement
Friction and wear behavior

ABSTRACT

In this study, defect-free and crack-free TiC_p/AZ31 composite coatings with a high TiC volume fraction (30–40 vol%) were successfully fabricated. The influence of the high ceramic volume fraction on the properties of these coatings was systematically investigated. The results reveal that a laser energy density of 40–60 W/mm^2 induces minimal dissolution of TiC particles in the molten pool, ensuring essential metallurgical reactions between the magnesium matrix and TiC. This process facilitates the formation of a semi-coherent interface between Mg and TiC while effectively suppressing the generation of defects such as porosity and cracks in the molten pool. As the TiC volume fraction increases, the microhardness of the TiC_p/AZ31 composite reaches 485 HV, representing a remarkable 766 % enhancement compared to the AZ31 matrix. Concurrently, the wear rate decreases by up to 74 % relative to the AZ31 matrix. The incorporation of TiC shifts the dominant wear mechanism of the magnesium matrix composite from adhesive wear to mild abrasive wear. The significant improvement in the wear resistance of the TiC_p/AZ31 composite coatings holds promise for providing a novel solution for the application of magnesium alloys in lightweight, wear-resistant composite materials.

1. Introduction

Magnesium alloys represent the lightest structural metallic materials for engineering applications; however, their insufficient hardness and wear resistance severely restrict broad applications in mechanical transmission systems, including gears, bearings, cams, and sliding guides [1–3]. Under frictional conditions, the soft magnesium matrix is prone to adhesive wear and thermal melting-induced wear from frictional heating, leading to rapid failure [4]. A critical challenge lies in effectively enhancing microhardness, wear and thermal resistance without compromising mechanical properties like yield strength. Particle-reinforced magnesium matrix composites have emerged as a viable approach for comprehensive performance enhancement, typically utilizing metallic or ceramic reinforcements. Metallic particles such as Ti [5], Al [6], and Li [7] effectively enhance strength-ductility synergy in magnesium matrix composites, yet their limited microhardness provides marginal wear rate reduction (typically <30 %) [8–10]. In the study by Ye et al. [8], Ti_p/AZ31 composites with 3–9 wt% (approximately 1.2–3.7 vol%) Ti particles were prepared via ultrasonic-assisted stir casting combined with hot extrusion. The composite containing 6 wt% Ti particles (~2.4 vol%) exhibited optimal performance, showing a 15 % increase in tensile strength and a 24 % improvement in elongation compared to the monolithic AZ31 alloy, while achieving a modest 5 % reduction in wear rate. In contrast, ceramic reinforcements including WC [11], TiN [12] SiC [13], and TiC [14–16] have proven more effective in simultaneously improving microhardness and wear resistance. TiC exhibits superior microhardness (~3100 HV) compared to other ceramic particles including WC (~2400 HV), TiN (~2100 HV), and SiC (~2500 HV), demonstrating distinct advantages for wear-resistant applications.

Furthermore, TiC possesses a melting point of approximately 3100 °C, which is significantly higher than that of most ceramic particles such as Al_2O_3 and SiC. This high melting point allows TiC to more effectively withstand the thermal effects generated during friction and

* Corresponding authors.
E-mail addresses: zhenzhengui@gzhu.edu.cn (Z. Gui), djliulyy@gmail.com (Y. Lu), zhf_jd@gzhu.edu.cn (F. Zhang), zhangtao@gzhu.edu.cn (T. Zhang).

https://doi.org/10.1016/j.surfcoat.2025.132466
Received 9 May 2025; Received in revised form 23 June 2025; Accepted 6 July 2025
Available online 7 July 2025
0257-8972/© 2025 Elsevier B.V. All rights are reserved, including those for text and data mining, AI training, and similar technologies.

wear. In a comparative study, Sahoo and Panigrahi [17] examined the wear morphology of TiC/AZ91 composites and the AZ91 matrix under conditions of high load (50 N) and high sliding speed (2 m/s). The AZ91 matrix exhibited substantial surface melting due to the accumulation of frictional heat, accompanied by evident features of adhesive tearing and oxidative spalling. In contrast, the TiC/AZ91 composite, benefiting from the high thermal stability and elevated melting point of TiC particles, effectively suppressed matrix softening. The worn surface of the composite showed only mild abrasive scratches and shallow pits, without significant signs of melting-related damage. On the other hand, compared to WC/Mg (8 %) [18], TiB_2/Mg (8.3 %) [19], and TiN/Mg (5.9 %) [20], TiC/Mg demonstrates a lower lattice mismatch (4.9 %) [21], which effectively reduces interfacial stress concentration and minimizes defect formation at the TiC/Mg interface, thereby enhancing interfacial bonding strength and load transfer efficiency. Combining these advantages, TiC is recognized as an ideal ceramic reinforcement for improving wear resistance in magnesium matrix composites. These combined advantages establish TiC as an ideal ceramic reinforcement for developing high-performance wear-resistant magnesium matrix composites.

The preparation methods for TiC particle-reinforced composites mainly include techniques such as mechanical stirring combined with self-propagating high-temperature synthesis (SHS). For instance, Xiu et al. [22] used this method to obtain TiC_p/AZ91 composites containing 5–15 wt% (approximately 1.9–6.1 vol%) TiC particles. The composite containing 15 wt% (approximately 6.1 vol%) TiC showed a reduction in wear volume of about 33 % compared with the AZ91 matrix. Wang [23] prepared TiC/Al-$Cu_{3.7}$-$Mg_{1.3}$ composites via 48-h mechanical ball milling of Al—$Cu_{3.7}$-$Mg_{1.3}$ alloy powder, Ti powder, and carbon nanotubes, followed by hot-press assisted hot extrusion. The 15 vol% TiC-reinforced composite demonstrated a 91 % microhardness enhancement and 37 % wear volume decrease compared to the matrix. Balraj [24] fabricated TiC/Mg composites via friction stir processing (FSP), achieving ~33 % lower wear rate than pure Mg. However, conventional methods face inherent limitations: powder metallurgy is constrained to small-scale production with prolonged ball milling requirements. Mechanical stirring and friction-based approaches often struggle with inhomogeneous particle distribution. In contrast, laser cladding has emerged as a promising alternative, enabling superior metallurgical bonding, precise process control, and rapid prototyping through pre-deposition or molten injection strategies [25,26]. Yang et al. [25] employed low-power pulsed laser cladding to apply a (Ti + B_4C) powder mixture onto AZ91D magnesium alloy, using a mass ratio of 5:1 and a total powder loading of 10–20 wt% (approximately 4.8–10.2 vol%). A TiC coating was formed in situ during the process. As the amount of mixed powder increased, the coating exhibited improvements in both microhardness and wear resistance by >50 %. Similarly, Pi et al. [26] applied TiC powder onto the surface of AZ31 using laser cladding, forming TiC-reinforced composite coatings with TiC contents ranging from 10 to 30 wt% (approximately 3.8–13.3 vol%). The coating with 30 wt% (approximately 13.3 vol%) TiC showed more than a 3.5-fold increase in microhardness compared to the AZ31 substrate.

Previous studies have demonstrated that high-volume-fraction ceramic particles offer significant advantages in enhancing the microhardness and wear resistance of coatings. For example, Li et al. [27] prepared TiC/Ni composites with 20–60 vol% TiC via direct laser fabrication (DLF), showing that 60 vol% TiC/Ni reduced wear volume by 63 % compared to 20 vol% TiC/Ni. Similarly, Chen et al. [28] reported a 73 % increase in hardness for 80 vol% TiC/H13 composites versus 30 vol% TiC/H13 via laser cladding. However, current research on laser melt-injected ceramic particle-reinforced magnesium matrix composites highlights a critical issue: TiC volume fractions in magnesium matrices are generally limited (<30 vol%) [25,26] compared to TiC-reinforced metallic systems such as TiC/Ni and TiC/Fe. This is primarily attributed to the significant coefficient of thermal expansion (CTE) mismatch between ceramic particles and magnesium alloys, the low melting point of magnesium alloys (~650 °C), and their high oxidation tendency, which exacerbate interfacial stress concentration and cracking risk at high ceramic contents (>30 vol%). For instance, Ghosh et al. [29] investigated the effect of SiC particle volume fraction on Al–4.5Cu–3 Mg metal matrix composites prepared by direct metal laser sintering (DMLS), finding that 30 vol% SiC increased microhardness by ~130 % compared to 10 vol% SiC. However, the CTE mismatch between SiC (7.4×10^{-6}/K) and the Al matrix (26×10^{-6}/K), combined with local stress concentration from particle agglomeration at high volume fractions, hinders effective load transfer to SiC particles, reducing the composite's load-bearing capacity. Therefore, further research is needed to develop crack-free and defect-free high-volume-fraction TiC_p/AZ31 coatings to overcome these process and interfacial bonding challenges.

This study prepared high-volume-fraction TiC_p/AZ31 coating by directly injecting spherical TiC particles into a high-temperature micro molten pool of hot-rolled AZ31 magnesium substrate via laser melt injection. Through precisely regulated inert gas shielding and synergistic control of laser parameters, powder feeding, and laser-powder interactions, rational thermal management of melt pool temperature and solidification rate was achieved, effectively mitigating defects such as cracks and porosity. Systematic investigations were conducted on the correlation between TiC particle distribution in weld overlays and laser processing parameters. The work further analyzed the interface characteristics between unmelted high-melting-point TiC particles and the AZ31 matrix, elucidating their formation mechanisms. Additionally, the influence mechanisms of high particle loading on wear resistance in TiC_p/AZ31 coating were comprehensively discussed, establishing process-structure-property relationships critical for high-performance coating design.

Table 1
Composition of the commercial hot-rolled AZ31 alloy (wt%).

Elements	Al	Zn	Mn	Si	Cu	Fe	Ni	Mg
Content	2.93	0.82	0.61	0.08	0.01	0.003	0.001	Bal.

2. Materials and methods

The commercial hot-rolled AZ31 magnesium alloy substrate was purchased from Beijing Global Jinxin International Technology Co., Ltd., with its chemical composition shown in Table 1. The spherical TiC particles were provided by Hunan Huawei Aerospace Special Materials Co., Ltd., with a particle size range of 15–53 μm. The scanning electron microscope (SEM) image and particle size distribution of the TiC particles are shown in Fig. 1. The detailed experimental procedure is as follows: TiC_p/AZ31 coatings were prepared using a 4 kW IPG YSL-4000 fiber laser. The initial 3 mm diameter laser beam was focused onto the surface of the AZ31 magnesium alloy substrate through an optical system. The spherical TiC particles were delivered by a dual-cylinder powder feeder, carried by argon gas through four separate channels, converging coaxially with the laser beam before entering the molten pool. The movement of the laser melt injection system was precisely controlled by a KUKA KRC4 robot. During the experiment, the number of TiC particles in the channel was precisely controlled by adjusting the carrier gas flow rate and the rotation speed of the feeding disc. Coaxial protection argon gas with a flow rate of 10 L/min was used to effectively suppress oxidation in the molten pool, ensuring the accuracy and stability of the experiment [30]. The TiC_p/AZ31 coating material prepared by multi-pass large-area overlap was calculated according to the laser volumetric energy density formula $E = P / DV$ [31] (where P is the laser power (W), D is the laser spot diameter (mm), and V is the laser scanning speed (mm/s)), with values of 40 W/mm^2 (1800 W/15 mm/s), 50 W/mm^2 (1500 W/10 mm/s), and 60 W/mm^2 (900 W/5 mm/s), respectively, and they were named E1, E2, and E3.

The cross-sections of the laser melt injection welds were cut, ground,

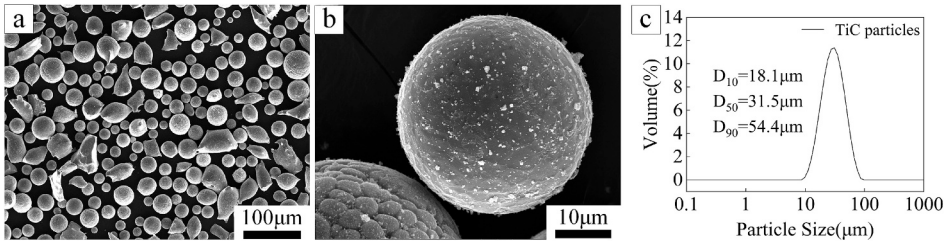


Fig. 1. (a, b) SEM images of TiC particles; (c) particle-size distribution of TiC particles.

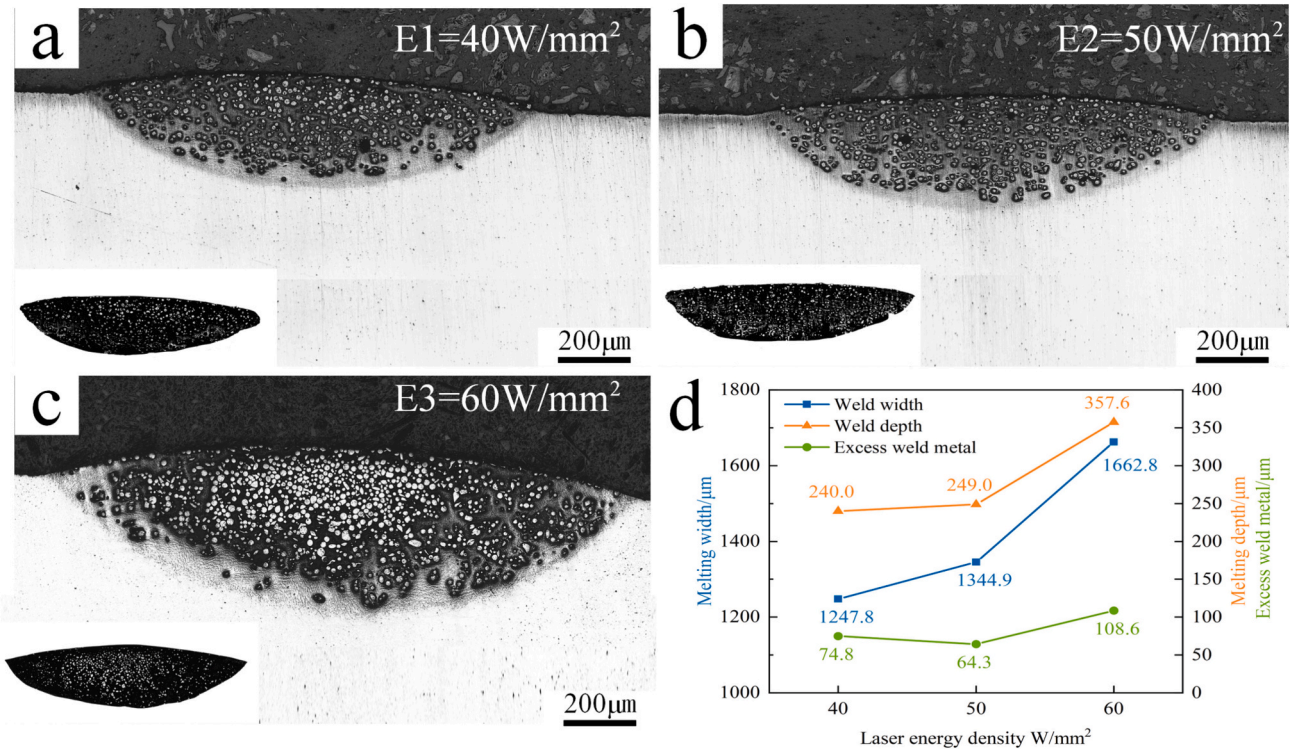


Fig. 2. Cross-sectional microstructure of the TiCp/AZ31 coating welds: (a) E1 single pass; (b) E2 single pass; (c) E3 single pass; (d) forming coefficient of TiCp/AZ31 melt-injected layers at different laser energy densities.

and polished for analysis. The microstructures of the samples were examined using an optical microscope (OM, Leica DM2700M) and a scanning electron microscope (Zeiss G460) equipped with a Bruker energy spectrometer. Performed using a Panalytical Empyrean X-ray diffractometer (Malvern Panalytical, The Netherlands). The instrument was operated with Cu Kα radiation at a tube voltage of 40 kV. XRD patterns were collected over a 2θ range of 30° to 80° at a scanning rate of 5°/min. The acquired diffraction data were analyzed using Jade 6 software and cross-referenced with standard PDF cards for phase identification. A Ga focused ion beam (FIB) scanning electron microscope (Thermo Scientific Scios 2) was used to prepare FIB–transmission electron microscopy (TEM) samples. The interfacial microstructure of the TiC_p/AZ31 coating was further characterized using a transmission electron microscopy (TEM, Thermo Fisher Talos F200X) equipped with an energy-dispersive X-ray spectrometer (EDS, SuperX G2142). Microhardness testing was conducted using a digital microhardness tester (HV-1000STA, Weiyi). The main test parameters were as follows: the indentation load was 200 gf, the loading time was 15 s, and the holding time was 15 s. Microhardness measurements were performed at 10 evenly spaced points along the same horizontal plane of the laser melt injection layer. The test area was divided into the following regions. Line A was located at 20 % of the total depth from the coating surface, representing the upper region. Line B was positioned at 50 % of the total depth, representing the microhardness characteristics of the central region. Line C was near the fusion line, marking the boundary between the TiC-melted layer and the AZ31 matrix. Line D was located on the AZ31 substrate, away from the heat-affected zone. Frictional wear testing was performed using a UMT-Tribolab frictional wear tester under the following conditions: an applied load of 20 N, a sliding speed of 10 mm/s, and a contact duration of 30 min in the presence of an Si_3N_4 friction ball. The worn surfaces of the samples were analyzed using a three-dimensional (3D) optical profiler (Micro1100, Raphael Optech) and a scanning electron microscope.

3. Results and analysis

3.1. Microstructure of TiC_p/AZ31 coating

To investigate the effect of different laser energy densities on the forming quality of the melt-injected layer of TiC_p/AZ31 coating materials, the OM morphology of the cladding cross-section of TiC_p/AZ31 coating was observed as shown in Fig. 2. As the laser energy density increased from 40 W/mm^2 (E1) to 60 W/mm^2 (E3), significant changes in the molten pool morphology were observed: the molten pool width increased from 1247.8 μm (E1) to 1662.8 μm (E3), and the molten depth increased from 240.0 μm to 357.6 μm. The increase in energy density

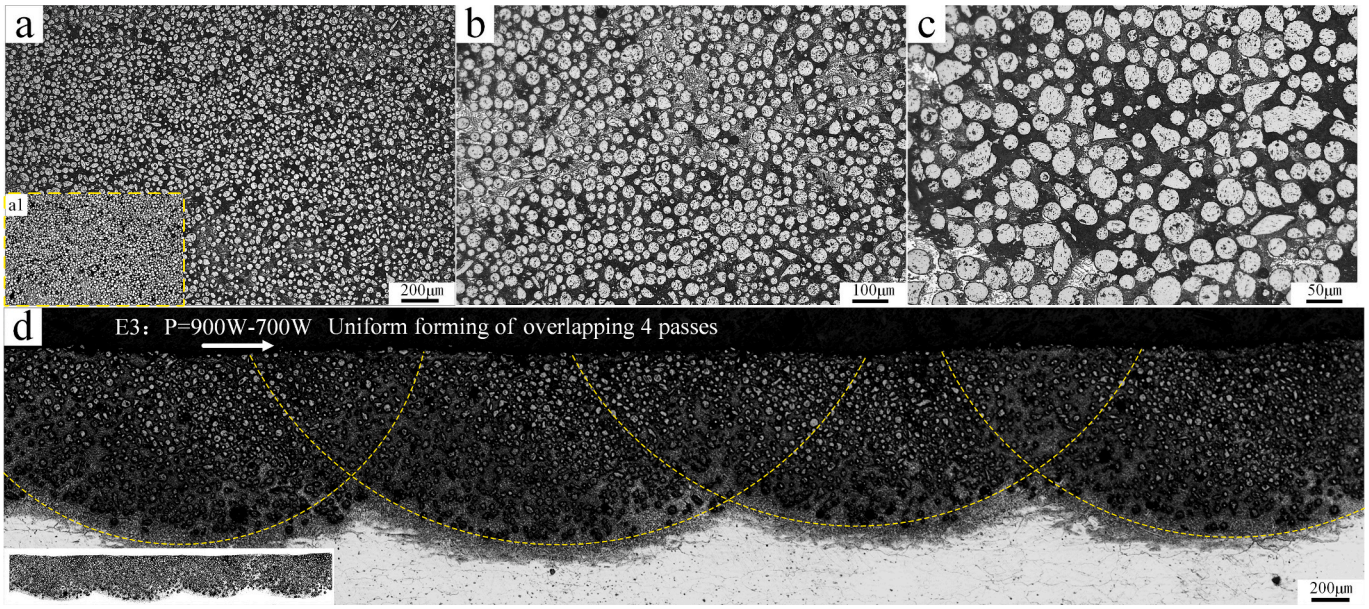


Fig. 3. OM images showing the morphologies of (a–c) particle distribution characteristics on the horizontal plane; (a1) corresponding binarized processed image of (a); (d) multi-pass lap weld.

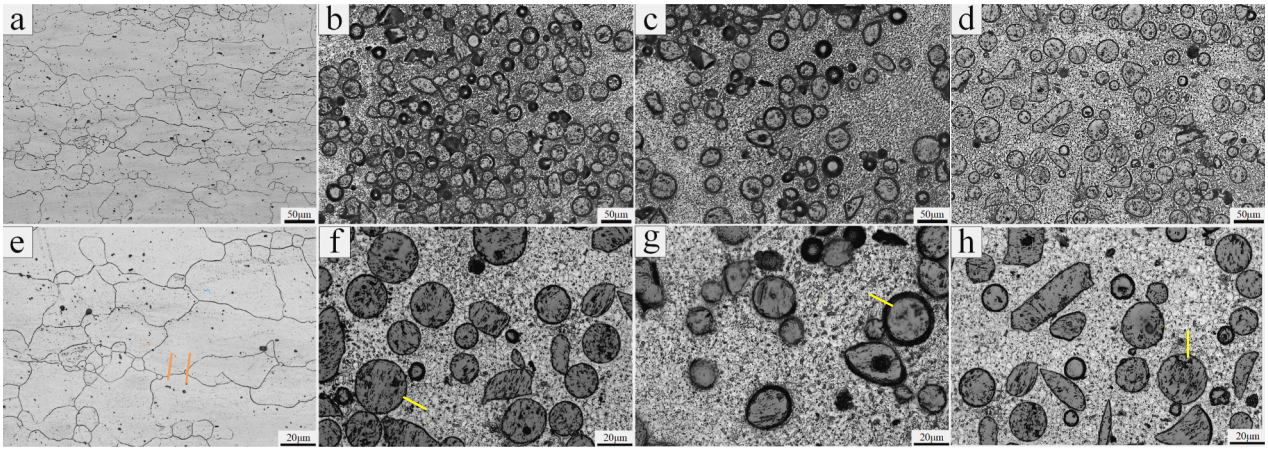


Fig. 4. OM images showing the morphologies of (a, e) hot-rolled AZ31, (b, f) E1, (c, g) E2, and (d, h) E3.

significantly enhanced the thermal input and expanded the melting region. Meanwhile, the results from binary thresholding calculations indicated that the volume fraction of TiC particles increased from 31.9 % (E1) to 39.2 % (E3) (as shown in the insets of Fig. 2(a–c)). The higher particle fraction at E3 could be attributed to the Marangoni convection [32], which promotes the lateral migration of particles under high energy density conditions.

As shown in Fig. 3(a–c), the TiC_p/AZ31 coating exhibits uniform surface particle distribution, with binarization analysis confirming 53 vol% TiC content in the upper layer (Fig. 3a1). Fig. 3(d) displays the OM morphology of multi-pass overlapping deposition, where specimens E1-E2-E3 demonstrate 30–40 vol% TiC fractions. Magnesium's low melting point and thermal accumulation effects during multi-pass processing significantly influence subsequent pool formation through residual heat transfer from prior tracks. Adjacent weld tracks undergo remelting-resolidification cycles under thermal cycling, necessitating strict control of pool stability for large-area fabrication. This study implemented adaptive power modulation (900 W–700 W) during multi-pass deposition, effectively mitigating pool collapse and crack formation from excessive temperatures. The controlled energy input maintained optimal solid-liquid interfacial energy balance, achieving continuous metallurgical bonding between successive tracks while preserving TiC distribution homogeneity across the deposited area.

As shown in Fig. 4, the effect of the laser energy density on the average grain size of the AZ31 matrix within the TiC_p/AZ31 coating was investigated. Grain-size statistics obtained using the intercept method indicated that the average grain size of α-Mg in the E1, E2, and E3 welds was significantly reduced from ~90 μm in the hot-rolled AZ31 matrix to ~9.5, ~7.5, and ~ 5.0 μm, respectively, as the laser energy density increased. This phenomenon is attributed to the rapid solidification effect under appropriate laser energy density conditions. The rapid heating and cooling process of laser melt injection inhibits grain growth. In addition, the TiC particles, as high-melting-point reinforcements, may have served as heterogeneous nucleation sites for the α-Mg phase during solidification, thereby promoting grain refinement [33]. After solidification, the pinning effect of TiC particles on grain boundaries further hinders grain growth. Consequently, the α-Mg grains in the TiC_p/AZ31 coating were significantly refined.

As shown in Fig. 5(a), the laser melt injection TiC_p/AZ31 layer had good coating formation quality The TiC particles retained their initial

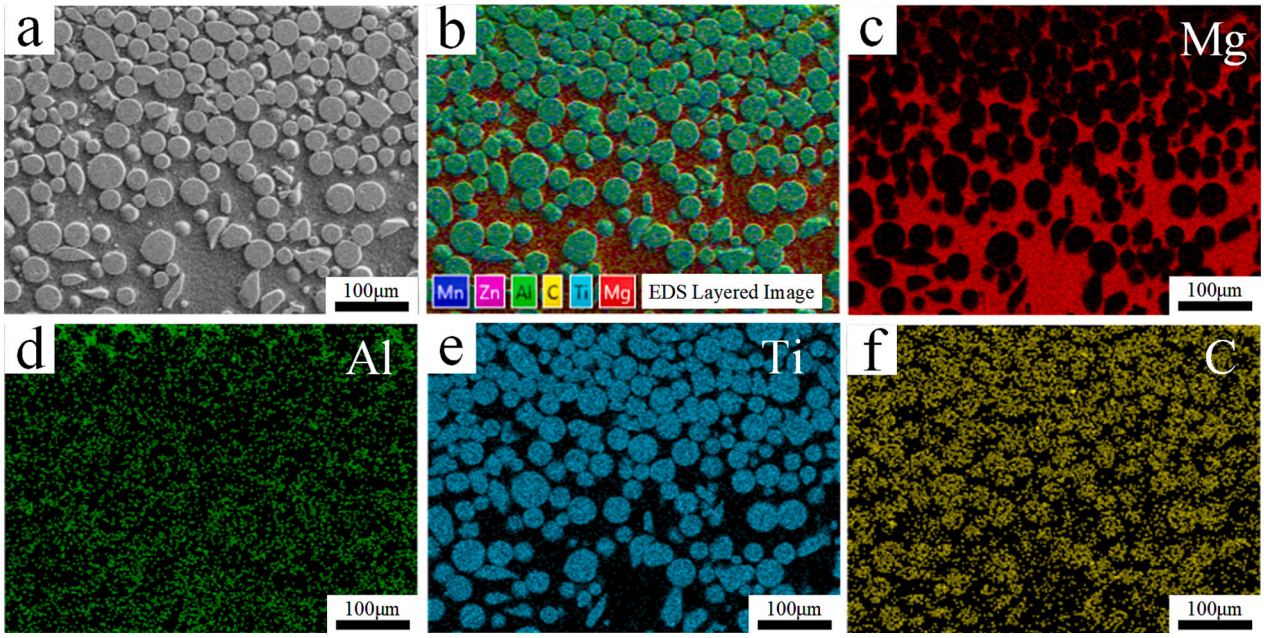


Fig. 5. SEM and EDS analysis of TiC_p/AZ31 coating: (a) SEM image; (b) EDS elemental distribution overlay; (c–f) elemental distributions of Mg, Al, Ti, and C.

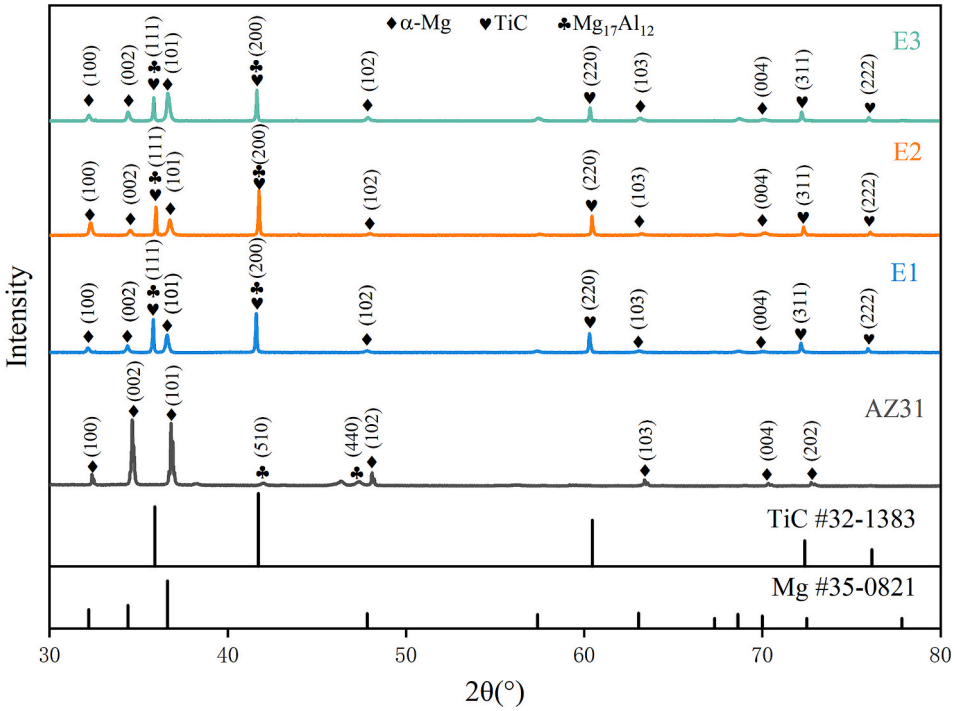


Fig. 6. XRD patterns of TiC_p/AZ31 coating prepared under different laser energy densities.

shape within the weld without signs of decomposition. Elemental mapping via EDS was employed to compare the distribution characteristics of Mg, Al, Ti, and C in the laser-cladded layer (Fig. 5c–f). Mg was found to be uniformly dispersed within the matrix, while Ti was concentrated within the TiC particles, indicating a well-confined intra-particle distribution. These observations suggest that no significant diffusion occurred for Mg and Ti during the cladding process. Although the quantitative accuracy of EDS for light elements is limited by its detection principles, Al and C exhibited relatively pronounced spatial fluctuations within the melt pool (Fig. 5d–f), in contrast to the stable distribution of Mg and Ti. The lattice mismatch between TiC and Al is only 5.9 % [33], and the resulting low interfacial energy may thermodynamically favor the ordered enrichment of Al atoms at low-energy sites along the TiC/Al interface. Additionally, considering the high thermal input during the laser cladding process, there appears to be a trend of C diffusing into the AZ31 matrix. However, to clarify whether Al and C undergo significant diffusion and to elucidate their diffusion mechanisms, further high-resolution TEM-EELS characterization is needed.

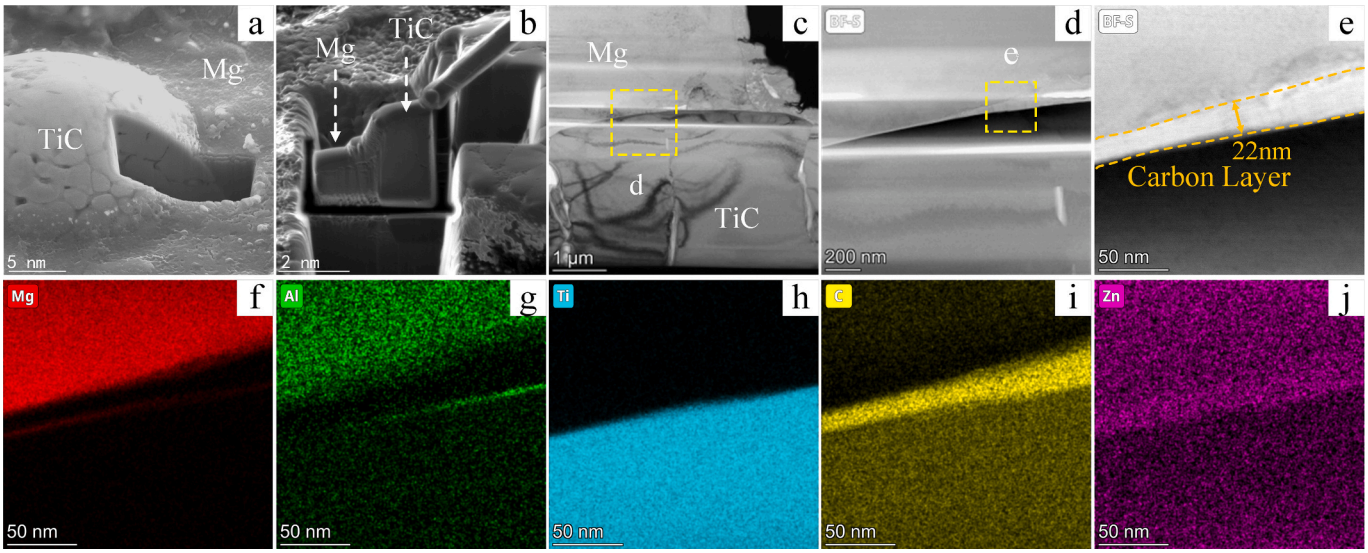


Fig. 7. (a, b) FIB-cut morphology of the interface between TiC particles and the Mg matrix; (c–e) BF images of the interface; (f–j) EDS mapping of elements at the interface: (f) Mg, (g) Al, (h) Ti, (i) C, and (j) Zn.

3.2. XRD analysis of TiC_p/AZ31 coating

The X-ray diffraction (XRD) phase analysis of the hot-rolled AZ31 matrix and TiC_p/AZ31 coating prepared under different laser energy conditions is shown in Fig. 6.The AZ31 matrix consisted of α-Mg (ICCD, PDF#35-0821) with a small amount of β-$Mg_{17}Al_{12}$ (PDF#73-1148). After the injection of TiC particles into the high-temperature micro-molten pool under laser irradiation, the XRD patterns of the TiC_p/AZ31 coating exhibited only the diffraction peaks of α-Mg, β-$Mg_{17}Al_{12}$, and pure TiC (ICCD, PDF#32-1382), with no obvious Ti or C peaks. XRD analysis did not reveal any characteristic diffraction peaks corresponding to free carbon (e.g., C, PDF#06-0675) or newly formed carbides. Combined with the localized carbon diffusion trend observed in the EDS mapping (Fig. 5f), this indirectly indicates that the extent of carbon diffusion was limited and insufficient to induce new phase formation or free carbon precipitation. Further characterization of the interfacial microstructure between TiC particles and the Mg matrix via TEM is required.

3.3. Interface bonding of TiC_p/AZ31 coating

Fig. 7(a)–(c) shows the FIB cutting process of TiC_p/AZ31 coating using a Ga FIB. Fig. 7(d) and (e) presents TEM bright-field (BF) images of the TiC particle–AZ31 matrix interface, and Fig. 7(f)–(j) presents the elemental distributions at a typical interface. As shown in Fig. 7(e), a C-enriched layer with an average thickness of approximately 22 nm existed at the interface between Mg and TiC particles. Adjacent to this layer was an Al-enriched layer with an average thickness of approximately 5 nm. No significant enrichment of Ti was detected. These findings are explained as follows: (i) The diffusion activation energy (E_a) of C in TiC_{1-y} is 39.5 kJ/mol (~0.4 eV/atom) [34], which is far lower than that of Ti (~7.65 eV/atom) [35] at the same temperature; i.e., C atoms require only a small kinetic energy to overcome the lattice potential barrier and migrate. In this study, the thermal energy from the high-energy laser beam during the laser melt injection process provided the activation energy for C diffusion. Even though the temperature of the molten pool is far lower than the melting point of TiC, C atoms can acquire sufficient thermal energy to drive diffusion. (ii) C diffusion can occur through C vacancies within TiC. TiC contains up to 50 % C vacancies, resulting in a C diffusion rate approximately 10^4 times that of Ti [36]. Therefore, under the high-temperature conditions of the laser melt injection pool, C from TiC preferentially diffuses to the interface between α-Mg and TiC, forming a C-enriched layer. The above results indicate that elemental diffusion occurs during laser melt injection, and potential chemical reactions may lead to the formation of Mg—C and Al-C-Ti compounds.

To further analyze the interfacial phases between Mg and TiC, high-resolution TEM (HRTEM) was employed. As shown in Fig. 8(a) and (b), regions I and II corresponded to C-rich transition layers formed between Mg and TiC. In Fig. 8(c), region III, located on the AZ31 side, was identified as Mg and Mg_2C_3 phases through fast Fourier transform (FFT) analysis (Fig. 8d) and diffraction-spot patterns (Fig. 8e). The corresponding d_1 and d_2 values were 0.524 and 0.272 nm, respectively, for Mg and 0.235 and 0.252 nm, respectively, for Mg_2C_3. The partial overlap of diffraction spots between Mg and Mg_2C_3 suggests a degree of lattice matching, indicating the presence of a semi-coherent orientation relationship between the two phases [37]. In addition, as shown in Fig. 8 (f), the lattice fringes corresponding to Mg_2C_3 revealed the presence of edge dislocations caused by lattice misalignment. The formation of edge dislocations may be attributed to stress concentrations induced by the significant mismatch in thermal expansion coefficients and lattice parameters between Mg and TiC, as well as the intrinsic driving force of the interfacial system to minimize its energy. These factors act synergistically to promote the development of high-density dislocation structures at the interface, thereby facilitating the accommodation of local stresses. With regard to stress relief mechanisms, Gao et al. [38] proposed that under specific thermomechanical processing conditions: such as slow cooling rates combined with intermediate temperature holding stages and interfacial stresses may be effectively relaxed via a heterogeneous recrystallization mechanism. This process favors grain boundary migration and the nucleation and growth of new grains. In contrast, the laser remelting process adopted in this study is characterized by an extremely high cooling rate. Coupled with the high thermal conductivity of the magnesium alloy substrate, the molten pool rapidly solidifies to room temperature within a very short time. These conditions severely inhibit atomic diffusion and grain boundary mobility, making it difficult to meet the critical time-temperature requirements for recrystallization. Consequently, no typical recrystallization features, such as equiaxed grains or recrystallization twins, were observed in the experiment. Instead, dislocation tangles were clearly observed near the TiC/Mg interface (see Fig. 8f), indicating that under the rapid solidification conditions employed in this study, interfacial stress is primarily released through dislocation-mediated localized plastic deformation rather than thermally activated recrystallization. Therefore, stress relaxation occurs via dislocation evolution rather than phase transformation, further

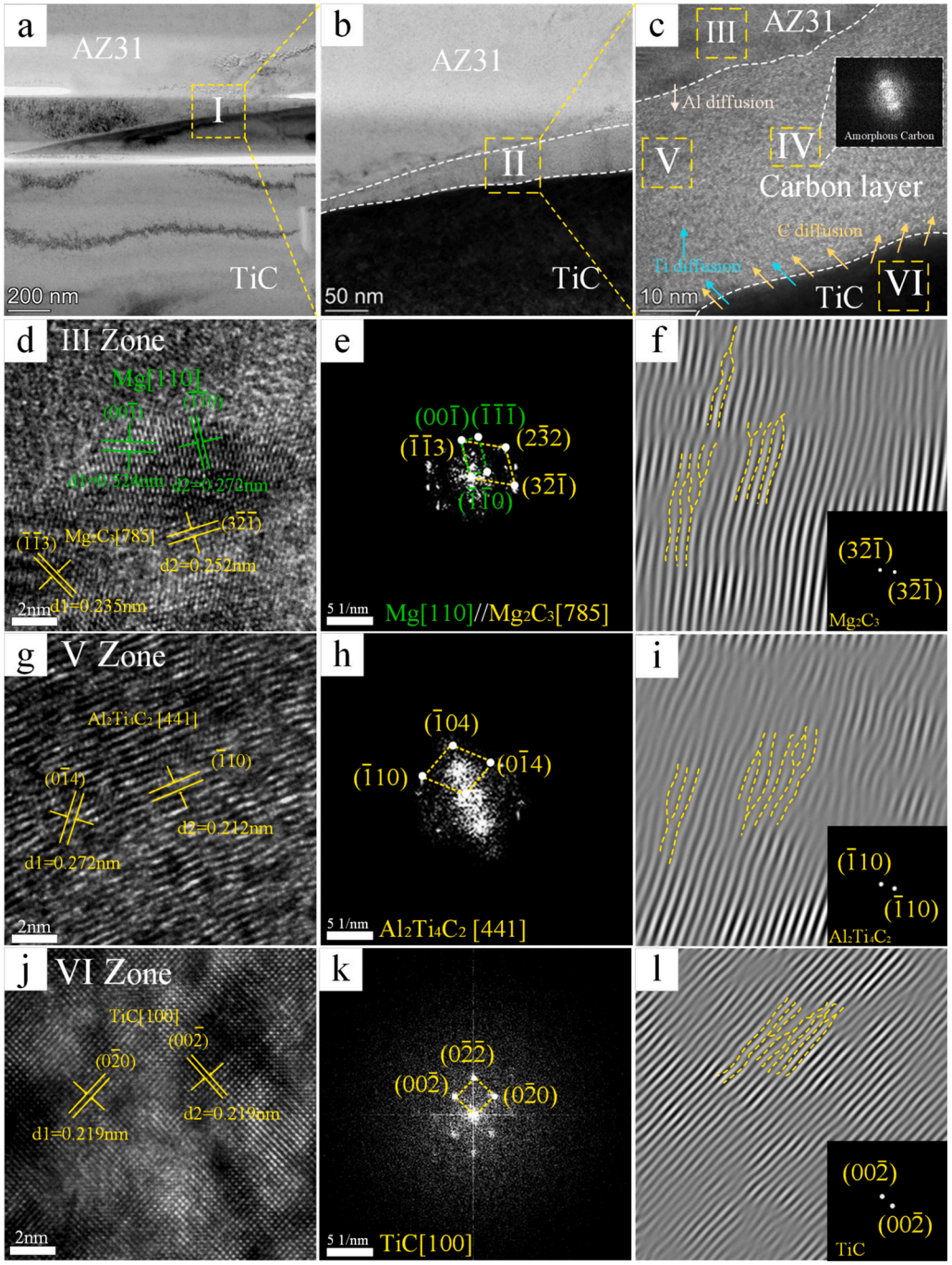


Fig. 8. (a–c) TEM images showing the morphology of the TiC particle–Mg matrix interface; the FFT result of the carbon layer in region m of (c) is shown in region IV; (d–f) HRTEM, FFT, and IFFT results for the Mg side; (g–i) HRTEM, FFT, and IFFT results for the region to the left of the carbon layer; (j–l) HRTEM, FFT, and IFFT results for the TiC region.

substantiating the mechanistic basis for the formation of edge dislocations. The dislocations release localized stress via slip, reducing the overall interfacial energy and maintaining the stability of the particle–matrix interface. FFT analysis of region IV in Fig. 8(c) indicates that the C layer had an amorphous ring pattern. The measured d_1 and d_2 values in region V (Fig. 8g) were 0.272 and 0.212 nm, respectively. Diffraction-spot analysis (Fig. 8h) confirmed that this phase corresponded to nanoscale $Al_2Ti_4C_2$, indicating that $Al_2Ti_4C_2$ formed at the C-enriched interface between Mg and TiC. This suggests that Ti from TiC and Al from the AZ31 Mg alloy underwent diffusion, which promoted the formation of the ternary compound $Al_2Ti_4C_2$ in the C-enriched region. In Fig. 8(c), the d_1 and d_2 values in region VI, measured in Fig. 8(j), are both 0.219 nm, corresponding to the standard lattice spacing of the TiC phase.

3.4. Mechanical properties

Fig. 9 shows the microhardness gradient of TiC_p/AZ31 coating from the surface to the substrate under different laser volumetric energy densities. Compared with the AZ31 matrix (~55 HV), the microhardness of the laser melt injection layer increased significantly with an increase in the laser volumetric energy density. For E1, E2, and E3, it reached maximum values of 415.7, 436.8, and 458.7 HV, respectively. The remarkable enhancement in microhardness of the TiC_p/AZ31 coating

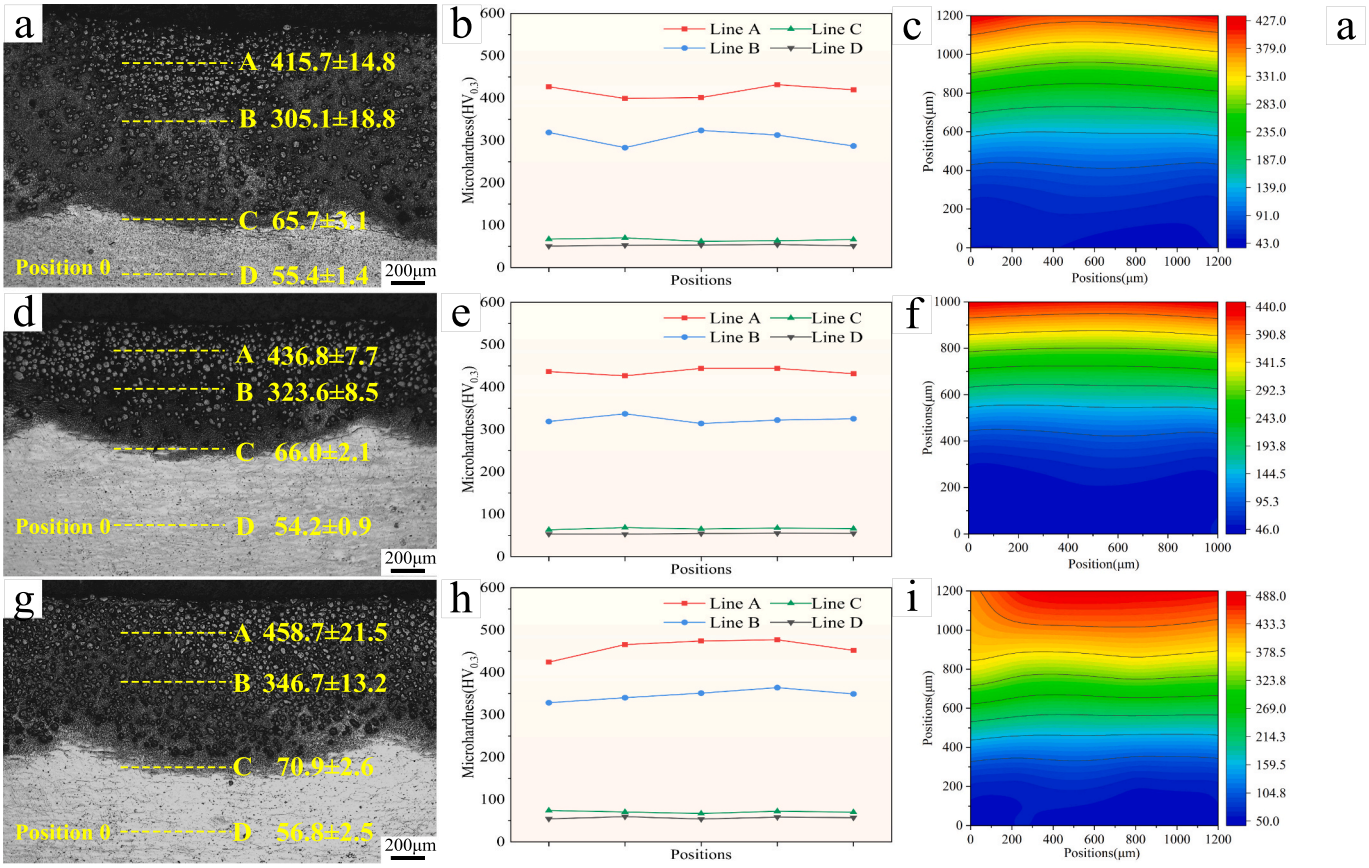


Fig. 9. Microhardness test locations, measurement results, and microhardness contour maps for TiC_p/AZ31 coating: (a–c) E1; (d–f) E2; (g–i) E3.

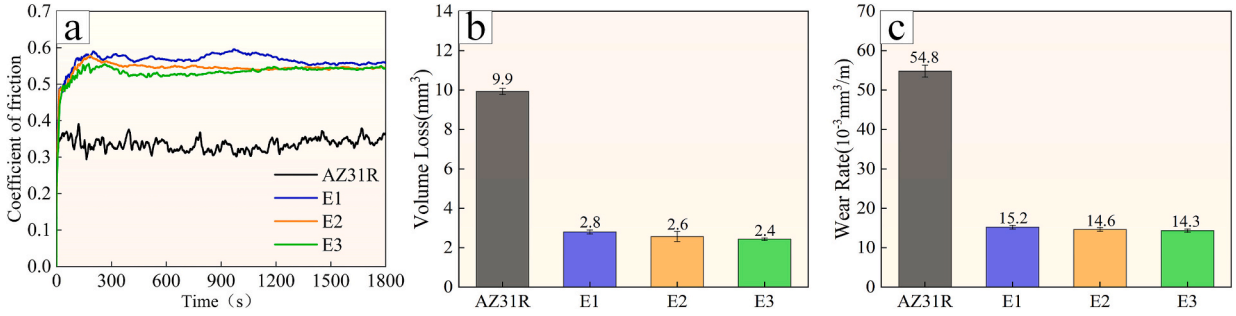


Fig. 10. (a) COF; (b) wear volume; (c) wear rate of the AZ31 matrix and TiC_p/AZ31 coating.

(766 % higher than the matrix) is ascribed to the synergistic effect of strong interfacial bonding between high-volume-fraction TiC particles and the magnesium alloy matrix, grain refinement strengthening induced by rapid laser solidification, and residual compressive stress generated by laser processing. TiC particles (hardness ~3100 HV) achieve strong bonding with the matrix via low lattice mismatch (4.9 %) with Mg and the formation of nanoscale Mg_2C_3 transition layers and semi-coherent interfaces during laser melt injection, not only enabling efficient external load transfer but also hindering dislocation motion through the Orowan mechanism [39]. Rapid laser solidification refines the AZ31 matrix grains from 90 μm in the hot-rolled state to 5 μm, significantly increasing the grain boundary area and substantially improving the material's plastic deformation resistance via the Hall-Petch effect [40]. Furthermore, appropriate heat input in the multi-track overlapping process of laser melt injection promotes a dynamic equilibrium of stress evolution [41]. Rational heat input resets the stress state through remelting, enhancing hardness by altering dislocation motion resistance. This significant positive correlation between residual compressive stress and microhardness further reinforces the deformation resistance of the coating via stress concentration effects in the fine-grained regions. To visually represent the microhardness gradient distribution of the TiC_p/AZ31 coating, the measured microhardness values were plotted as microhardness contour maps, as shown in Fig. 9(c), (f), and (i). In these diagrams, high-hardness regions are represented in red, and the matrix appears in blue.

The test results of the coefficient of friction (COF), wear volume, and wear rate for hot-rolled AZ31 and TiC_p/AZ31 coatings processed at different laser energy densities are shown in Fig. 10. As depicted in Fig. 10(a), the COF of AZ31 fluctuates periodically between 0.31 and 0.38 throughout the 0–1800 s testing period. By contrast, the TiC_p/AZ31 coatings exhibit a COF of approximately 0.55, with almost no fluctuation after 1200 s, indicating a more stable wear stage. Fig. 10(b) and (c) shows that the wear volume and wear rate of TiC_p/AZ31 coatings are significantly lower than those of the hot-rolled AZ31 matrix.

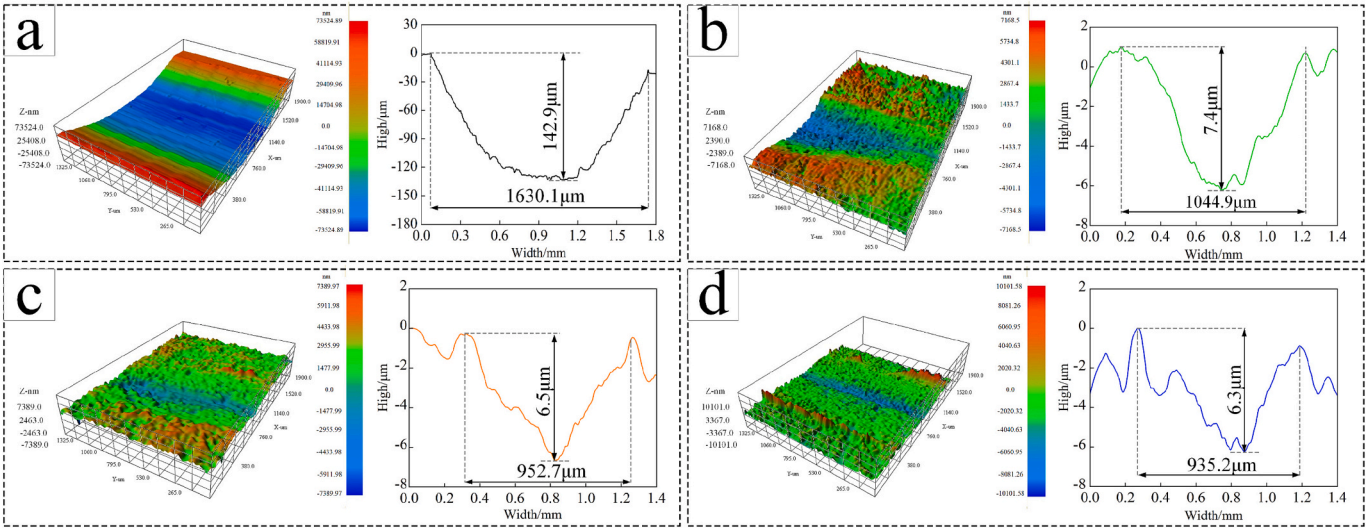


Fig. 11. 3D morphology of worn surfaces and the corresponding cross-sectional profiles for the AZ31 matrix and TiC_p/AZ31 coating: (a) AZ31R; (b) E1; (c) E2; (d) E3.

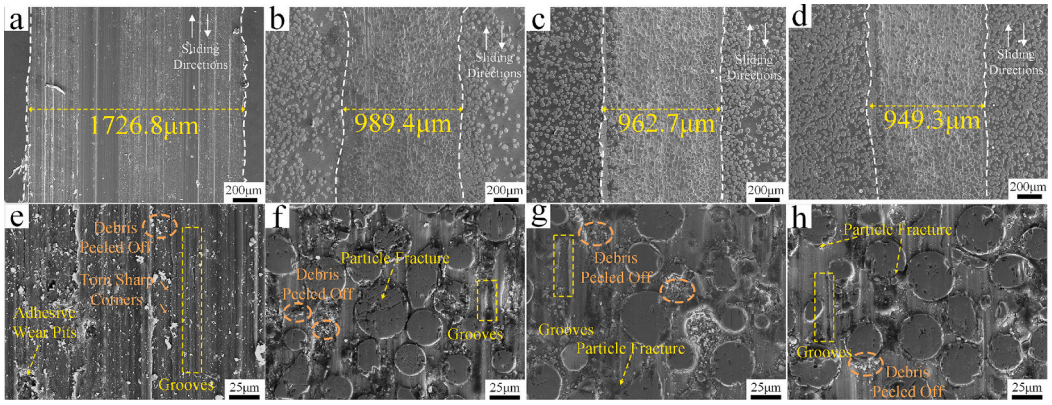


Fig. 12. SEM images of worn surfaces: (a, e) hot-rolled AZ31; (b, f) E1; (c, g) E2; (d, h) E3.

Specifically, the wear volume and wear rate of TiC_p/AZ31 coatings prepared at different laser energy densities are reduced by 71.7 %, 73.7 %, and 75.6 %, and 72.3 %, 73.4 %, and 73.9 %, respectively. Fig. 11 illustrates the 3D morphology of the worn surface and its corresponding cross-sectional profiles. The width of the wear track decreases with increasing laser energy density. Compared with the hot-rolled AZ31 matrix, the maximum reductions in the width and depth of the wear track for TiCp/AZ31 coatings are 42.6 % and 95.6 %, respectively.

To investigate the differences in friction-wear mechanisms between TiC_p/AZ31 coating and AZ31 matrix, SEM observations were conducted on their respective worn surfaces. As shown in Fig. 12(a,e), the AZ31 matrix exhibited large torn edges, wide wear tracks (1726.8 μm), and parallel grooves caused by severe plastic deformation. The EDS point analysis results of the fragment particles in Fig. 12(e) show that their main compositions are Mg (~73.1 %) and O (~25.6 %). Although EDS has some errors in the quantitative analysis of light elements such as oxygen, combining the observed typical flake morphology characteristics and the fact that the AZ31 matrix is prone to oxide formation under dry sliding conditions, we speculate that Mg-type products may have been generated during the wear process. This phenomenon suggests that oxidative wear and adhesive wear may dominate the wear mechanism of AZ31 matrix.

As evident from Fig. 12(b–d), the TiC_p/AZ31 coatings showed significantly narrowed wear tracks compared to AZ31, with wear track width further reduced to 949.3 μm as TiC volume fraction increased. This improvement is attributed to stress dispersion by high TiC content during friction-wear processes, preventing localized overloading. Fig. 12 (f–h) reveals shallower grooves in the coatings versus the matrix, with partial TiC particle fracture but no detachment. The strong metallurgical bonding between Mg and Mg_2C_3 through semi-coherent orientation relationships not only enhances interfacial strength but also improves coating hardness via the hard Mg_2C_3 phase (Fig. 8(d–f)). Although fragmented TiC particles act as third-body abrasives, their detrimental effects are outweighed by the coating's superior microhardness and interfacial bonding, resulting in a wear mechanism transition to mild abrasive wear and oxidative wear.

The apparent contradiction that the composite coating exhibits an increased coefficient of friction (COF, ΔCOF≈0.15) but a 75.6 % reduction in wear rate essentially reveals the nonlinear correlation between COF and wear resistance. As a quantitative parameter of tangential resistance during contact surface motion ($\mu = F_f / F_N$), the dynamic evolution of COF (e.g., initial fluctuation, stable plateau, and late-stage mutation) reflects the interfacial interaction process rather than directly mapping wear resistance. For instance, low COF may exacerbate wear: Ji et al. [42] prepared MoS_2 coatings on iron substrates and found that increasing MoS_2 content reduced COF via lubricating transfer film formation and transition from two-body to three-body wear, but the low hardness of MoS_2 weakened the matrix strength and aggravated wear. Conversely, high COF can inhibit material loss due to hard phase support or strong interfacial bonding, as seen in this study

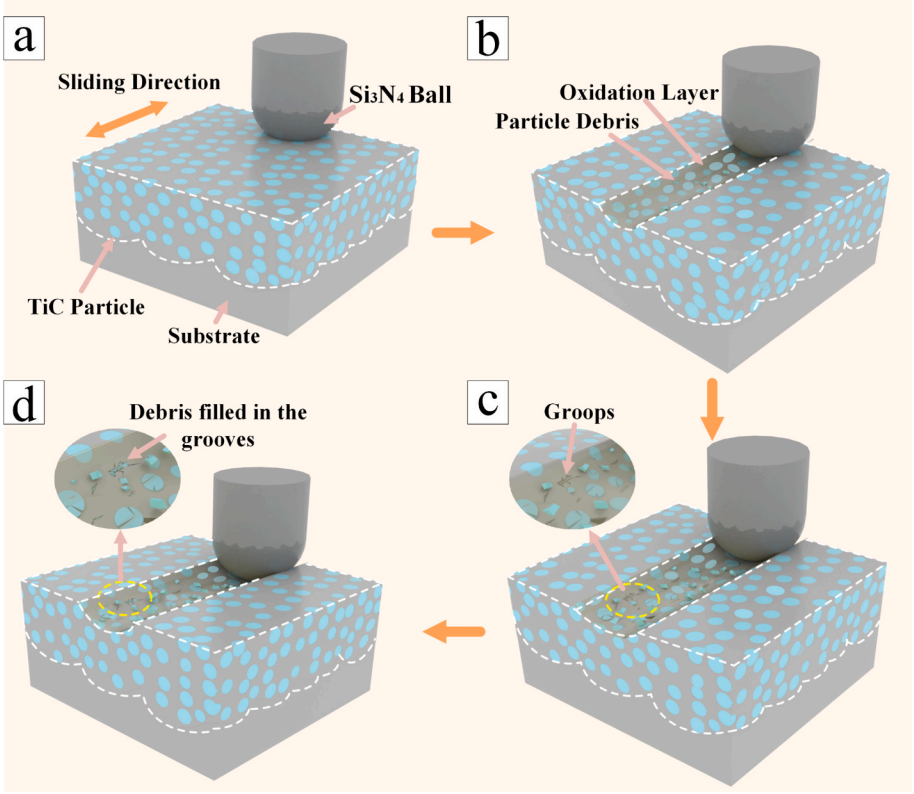


Fig. 13. Schematic of the sliding wear mechanism of the TiC_p/AZ31 coating.

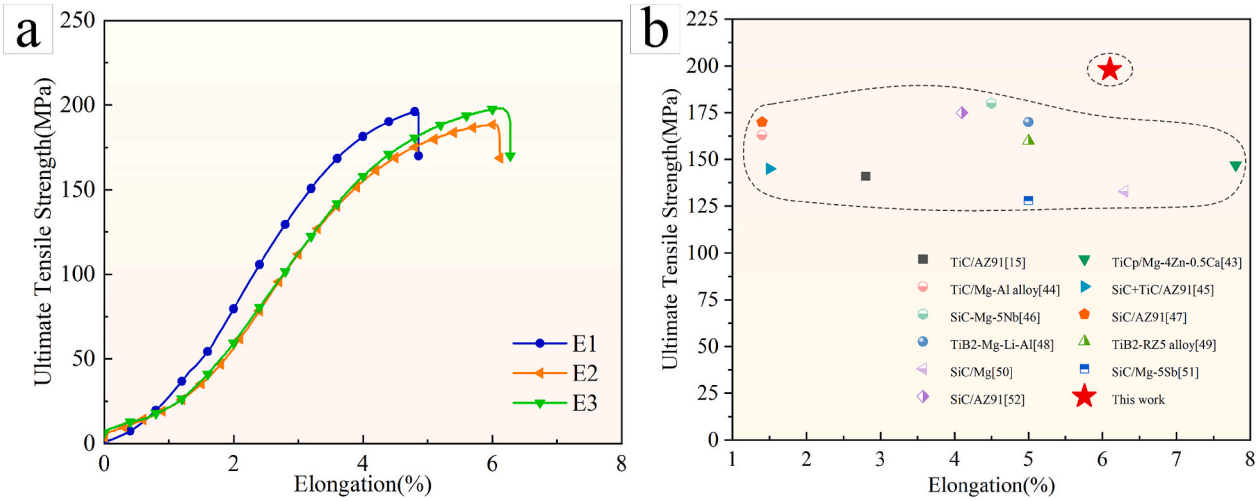


Fig. 14. (a) TiC_p/AZ31 coating fabricated under different laser volumetric energy densities; (b) comparison of the tensile properties of TiC_p/AZ31 coating with data from other studies [15,43–52].

where the TiCp/AZ31 coating shows higher COF than the AZ31 matrix but significantly lower wear rate. From the perspective of the composite's friction-wear process, as shown in Fig. 13(a–b), preferential wear of the soft AZ31 matrix at the initial stage creates a significant interfacial height difference between TiC particles and the matrix, causing the friction pair to contact hard TiC particles preferentially, which elevates COF while protecting the matrix. With prolonged wear, repeated impacts from the friction pair induce local brittle fracture of TiC particles, generating submicron irregular debris (Fig. 13(b–c)). These fragmented TiC particles may act as third-body abrasives, scratching the coating surface and causing COF fluctuations. At the advanced wear stage, the fragmented TiC particles mechanically interlock with the Mg matrix, stabilizing COF and blocking direct contact between the friction pair and matrix, thereby reducing wear loss (Fig. 13(c–d)).

Table 2
Tensile properties of TiC_p/AZ31 coating and hot-rolled AZ31.

Samples	YS/MPa	UTS/MPa	EL/%
E1	80.3 ± 2.2	195.5 ± 4.7	4.8 ± 0.9
E2	77.8 ± 3.1	188.3 ± 5.1	6.0 ± 1.1
E3	80.4 ± 2.9	197.3 ± 3.9	6.1 ± 1.2

Fig. 14(a) presents a typical engineering stress–strain curve of the

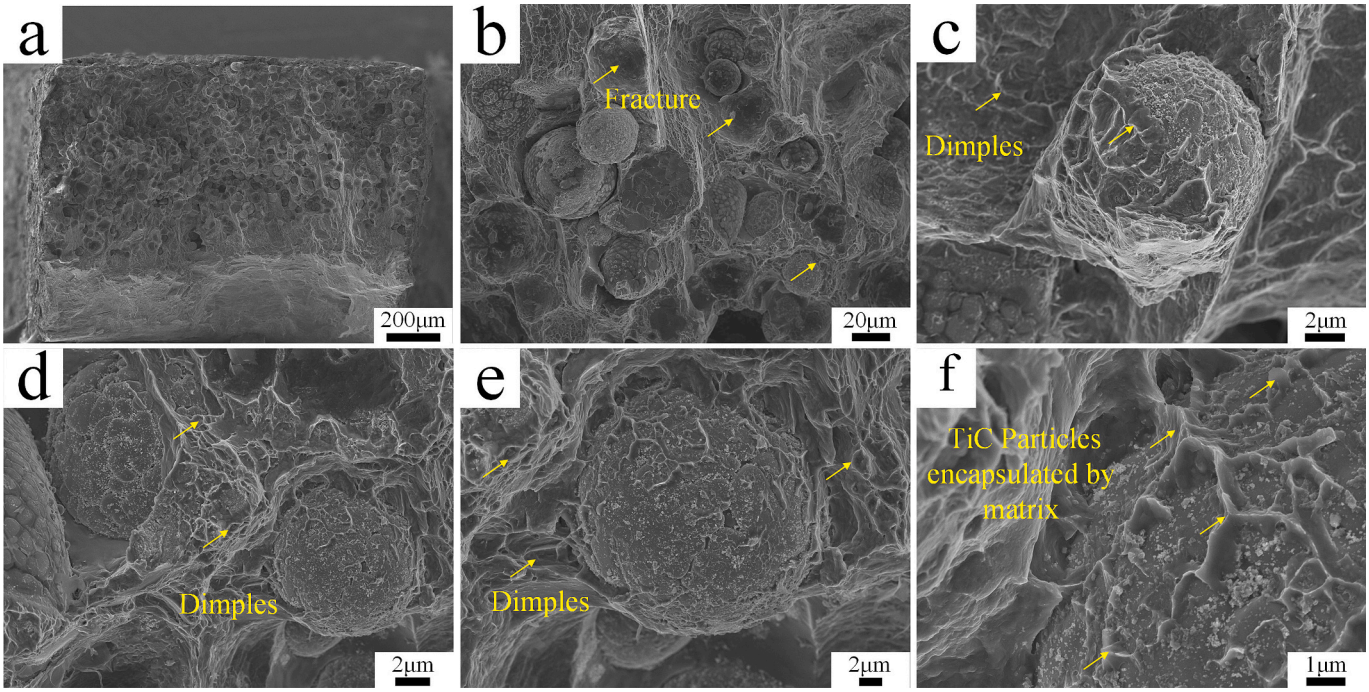


Fig. 15. Typical fracture characteristics of TiC_p/AZ31 coating: (a) overall fracture morphology; (b) typical fracture surface features; (c–f) fracture morphology showing dimples in the matrix.

TiC_p/AZ31 coating. As shown in Table 2, with increasing laser volumetric energy density, the TiC_p/AZ31 coating had excellent overall tensile properties, with a yield strength (YS) of approximately 80.4 MPa, an ultimate tensile strength (UTS) of approximately 197.3 MPa, and an elongation (EL) of approximately 6.1 %. As shown in Fig. 12(b) [15,43–52], the UTS and EL of TiC_p/AZ31 coating were compared with those of other metal–matrix coating featuring either typical as-cast microstructures or those formed through laser rapid solidification. Although the TiC/Mg-4Zn-0.5Ca coating [43], which was fabricated via mechanical stirring followed by extrusion molding, achieved an EL of approximately 7.8 %, the agglomeration of TiC particles led to a relatively low UTS of only 147 MPa. This highlights the difficulty of simultaneously achieving both high tensile strength and good elongation. In contrast, in the present study, TiC_p/AZ31 coating with a uniform distribution of TiC particles and strong metallurgical bonding at the TiC/matrix interface were produced by optimizing the laser processing parameters and powder feeding techniques. As a result, the coating had superior overall mechanical properties.

As shown in Fig. 15(a), the overall fracture morphology revealed the presence of tear ridges and dimples, along with a small number of dispersed circular pores. These features indicated significant plastic deformation of the AZ31 matrix during fracture which is a key characteristic of transgranular fracture. As shown in Fig. 15(b), the fracture surface of the coating contained pull-out cavities of TiC particles and fractured TiC particles. The presence of fractured TiC particles confirmed that the TiC/matrix interface maintained strong metallurgical bonding during tensile loading, allowing the interface to withstand high tensile stress. As shown in Fig. 15(c)–(f), Mg alloy surrounded the TiC particles, and dimples formed by matrix tearing were observed on the particle surfaces. This suggests that the TiC/AZ31 interface effectively transferred load during tensile deformation. The results provide additional evidence of the excellent metallurgical bonding between the reinforcing TiC particles and the AZ31 matrix in the coating.

4. Conclusions

This study investigated the influence of high ceramic volume fraction on the properties of TiC_p/AZ31 composite coatings fabricated via laser melt injection (LMI). The results indicate that optimized laser processing parameters (40–60 W/mm^2) ensured the necessary metallurgical reaction between the magnesium matrix and TiC particles while simultaneously suppressing the formation of defects and cracks. The rapid solidification induced by the laser at this energy density range refined the AZ31 matrix grains from 90 μm (as-rolled state) to 5 μm. Furthermore, nano-scale Mg_2C_3 precipitates and a carbon-rich layer facilitated the formation of a semicoherent interface between TiC and the magnesium matrix. With increasing TiC volume fraction, the microhardness of the TiC_p/AZ31 composites reached 485 HV, representing a 766 % enhancement (or a 7.6-fold increase) compared to the matrix. Additionally, the wear rate decreased by up to 74 % relative to the AZ31 substrate. Consequently, the incorporation of TiC transformed the dominant wear mechanism of the magnesium matrix composites from adhesive wear to mild abrasive wear. The significant improvement in the wear resistance of the TiC_p/AZ31 composite coatings holds promise for providing a novel solution for the application of magnesium alloys in lightweight, wear-resistant composite materials.

CRediT authorship contribution statement

Zhenzhen Gui: Writing – review & editing, Writing – original draft, Supervision, Project administration, Methodology, Funding acquisition. **Pengxi Liu:** Writing – review & editing, Writing – original draft, Funding acquisition, Data curation. **Keying Zhu:** Investigation, Data curation. **Yuanyuan Lu:** Writing – review & editing, Supervision, Methodology. **Chaowen Guo:** Investigation, Data curation. **Tao Zou:** Supervision, Methodology, Funding acquisition. **Liu Cao:** Investigation, Formal analysis. **Fan Zhang:** Writing – review & editing, Supervision, Methodology. **Tao Zhang:** Project administration, Methodology, Funding acquisition, Conceptualization. **Dejian Liu:** Resources, Investigation.

Declaration of competing interest

The authors declare that they have no known competing financial

interests or personal relationships that could have appeared to influence the work reported in this paper.

Acknowledgments

This work was financially supported by the Guangdong Basic and Applied Basic Research (No. 2022A1515010265), Science and Technology Planning Project of Guangdong Province (2024A0505040017), the Science and Technology Program of Guangzhou City Joint with Universities (No. 2025A03J3107). the National Natural Science Foundation of China (No. 52371104), the Research and Integrated Application of Hardware Knife and Shear Materials, Forming Processing and Equipment Control Technology (No. RCZX2023003).

Data availability

Data will be made available on request.

References

[1] Z. Wei, H. Dong, J. Zhang, R. Wu, Y. He, R. Bao, X. Zhang, J. Wang, Preparation of high strength mg–Li–Zn–Y alloy by MgLi2Zn precipitation, Mater. Sci. Eng. A 890 (2024) 145842.
[2] T. Shen, H. Liu, J. Zhang, M. Ma, Z. Wu, L. Liu, L. Lu, The improvement on mechanical anisotropy of AZ31 magnesium alloy sheets by multi cross-rolling process, J. Alloys Compd. 963 (2023) 171252.
[3] J. Yang, Z. Zhu, S. Han, Y. Gu, Z. Zhu, H. Zhang, Evolution, limitations, advantages, and future challenges of magnesium alloys as materials for aerospace applications, J. Alloys Compd. 1008 (2024) 176707.
[4] C. Taltavull, P. Rodrigo, B. Torres, A.J. Lopez, J. Rams, Dry sliding wear behavior of AM50B magnesium alloy, Mater. Des. 56 (2014) 549–556.
[5] D. Pu, S. Wu, H. Yang, X. Chen, J. Li, X. Feng, F. Pan, Effect of Ti particles on microstructure and mechanical properties of TiP/AZ91 composites, J. Mater. Res. Technol. 22 (2023) 1362–1374.
[6] S. Zhong, D. Zhang, Y. Wang, S. Chai, J. Feng, Y. Luo, F. Pan, Microstructures, mechanical properties and degradability of Mg-2Gd-0.5 (Cu/Ni) alloys: a comparison study, J. Mater. Sci. Technol. 128 (2022) 44–58.
[7] Y. Wang, R. Wu, N. Turakhodjaev, M. Liu, Microstructural evolution, precipitation behavior and mechanical properties of a novel Al–Zn–mg–cu–Li–Sc–Zr alloy, J. Mater. Res. 36 (3) (2021) 740–750.
[8] J. Ye, X. Chen, H. Luo, J. Zhao, J. Li, J. Tan, H. Yang, B. Feng, K. Zheng, F. Pan, Microstructure, mechanical properties and wear resistance of Ti particles reinforced AZ31 magnesium matrix composites, Journal of Magnesium and Alloys. 10 (8) (2022) 2266–2279.
[9] Q. Chen, Z. Zhao, Z. Zheng, G. Cheng, Y. Zhao, L. Lu, Effects of Al content on friction and wear behavior of weld surfacing mg-Al-Zn alloy, Metall. Mater./ Kovové Mater. 58 (1) (2020).
[10] Y. Wang, S. Chen, Y. Zhang, Y. Bai, Z. Fang, T. Cui, X. Sun, Effects of post heat treatment on key T-phase evolution and the matching mechanism of enhanced strength-toughness, wear resistance and corrosion resistance in Al-mg-Zn-(cu-Er-Zr) alloy by laser powder bed fusion, J. Alloys Compd. 1005 (2024) 175976.
[11] S. Banerjee, S. Poria, G. Sutradhar, P. Sahoo, Tribological behavior of mg-WC nanocomposites at elevated temperature, Mater. Res. Express 6 (8) (2019) 0865c6.
[12] T. Sathish, L. Kamaraj, V. Mohanavel, Y. Jazaa, F. Qahtani, S. Althahban, A novel technique implementation to fabricate and analysis of AZ91D with TiN through FSP, Int. J. Adv. Manuf. Technol. (2023) 1–16.
[13] X. Liu, T. Feng, X. Meng, S. Wen, W. Hou, J. Ding, H. Lin, Z. Yue, Effect of SiC nanowires on adhesion and wear resistance of hydroxyapatite coating on AZ31 magnesium alloy, J. Alloys Compd. 960 (2023) 170934.
[14] F. Aydin, Y. Sun, M. Emre Turan, Influence of TiC content on mechanical, wear and corrosion properties of hot-pressed AZ91/TiC composites, J. Compos. Mater. 54 (2) (2019) 141–152.
[15] A. Kumar, S. Kumar, N. Mukhopadhyay, A. Yadav, D. Sinha, Effect of TiC reinforcement on mechanical and wear properties of AZ91 matrix composites, Int. J. Metalcast. 16 (4) (2022) 2128–2143.
[16] A.K. Das, R. Kumar, Investigation on Tribological Characteristics of Plasma Transferred Arc Cladded Co-TiC-CaF2 Metal Matrix Composite Coating Produced on Magnesium Alloy AZ91D Substrate, J. Therm. Spray Technol. (2025) 1–23.
[17] B.N. Sahoo, S.K. Panigrahi, Development of wear maps of in-situ TiC+ TiB_2 reinforced AZ91 Mg matrix composite with varying microstructural conditions, Tribol. Int. 135 (2019) 463–477.
[18] X. Li, Y. Li, J. Xu, J. Gong, Y. Wang, Z. Chen, Effect of alloying elements on interfacial properties and mechanical behavior of mg/WC systems: a first-principles study, Comput. Mater. Sci. 232 (2024) 112630.
[19] P. Xiao, Y. Gao, F. Xu, S. Yang, B. Li, Y. Li, Q. Zheng, An investigation on grain refinement mechanism of TiB_2 particulate reinforced AZ91 composites and its effect on mechanical properties, J. Alloys Compd. 780 (2019) (2019) 237–244.
[20] T. Yang, M. Wei, Z. Ding, X. Han, J. Li, Ab initio calculations on the mg/TiN heterogeneous nucleation interface, J. Phys. Chem. Solid 143 (2020) 109479.
[21] T.Y. Tan, J. Li, S.Y. Gao, A first principles investigation on the mechanism of TiC act as heterogeneous nucleation substrate of mg phase to refine grains in AZ91, AIP Adv. 9 (8) (2019).
[22] K. Xiu, H.Y. Wang, H.L. Sui, Y. Wang, C.L. Xu, J.G. Wang, Q.C. Jiang, The sliding wear behavior of TiC_p/AZ91 magnesium matrix composites, J. Mater. Sci. 41 (2006) 7052–7058.
[23] L. Wang, B. Dong, F. Qiu, R. Geng, Q. Zou, H. Yang, Q. Jiang, Dry sliding friction and wear characterization of in situ TiC/Al-$Cu_{3.7}$-$Mg_{1.3}$ nanocomposites with nacre-like structures, J. Mater. Res. Technol. 9 (1) (2020) 641–653.
[24] B. Singh, J. Singh, R.S. Joshi, Effect of tic reinforcement on wear resistance of magnesium matrix composite by Fsp, Arch. Metall. Mater. (2022) 293–302.
[25] L. Yang, Z. Li, Y. Zhang, S. Wei, F. Liu, Al-TiC in situ composite coating fabricated by low power pulsed laser cladding on AZ91D magnesium alloy, Appl. Surf. Sci. 435 (2018) 1187–1198.
[26] H. Pi, G. Zhi, C. Chen, C. Li, J. Zhou, Y. Long, Microstructure, hardness and corrosion resistance of Al-TiC MMC prepared by laser cladding on AZ31B magnesium alloy, Coatings 14 (2) (2024) 211.
[27] Y. Li, P. Bai, Y. Wang, J. Hu, Z. Guo, Effect of TiC content on Ni/TiC composites by direct laser fabrication, Materials & Design. 30 (4) (2009) 1409–1412.
[28] H. Chen, Y. Lu, Y. Sun, Y. Wei, X. Wang, D. Liu, Coarse TiC particles reinforced H13 steel matrix composites produced by laser cladding, Surf. Coat. Technol. 395 (2020) 125867.
[29] S.K. Ghosh, P. Saha, S. Kishore, Influence of size and volume fraction of SiC particulates on properties of ex situ reinforced Al–4.5 cu–3Mg metal matrix composite prepared by direct metal laser sintering process, Mater. Sci. Eng. A, Struct. Mater. Prop. Microstruct. Process. 527 (18–19) (2010) 4694–4701.
[30] Z. Gui, Y. Lu, H. Chen, L. Cao, Z. Kang, G. Wen, D. Liu, Preparation and properties of Ti_p/mg-RE composites through laser melt injection, Mater. Sci. Eng. B 287 (2023) 116095.
[31] R. Molian, P. Shrotriya, P. Molian, Thermal stress fracture mode of CO_2 laser cutting of aluminum nitride, Int. J. Adv. Manuf. Technol. 39 (7–8) (2007) 725–733.
[32] S. Khairallah, A. Anderson, A. Rubenchik, W. King, Laser powder-bed fusion additive manufacturing: physics of complex melt flow and formation mechanisms of pores, spatter, and denudation zones, Acta Mater. 108 (2016) 36–45.
[33] A.E. Karantzalis, A. Lekatou, E. Georgatis, H. Mavros, Solidification behaviour of ceramic particle reinforced Al-alloy matrices, J. Mater. Sci. 45 (2010) 2165–2173.
[34] F. Vanloo, W. Wakelkamp, G. Bastin, R. Metselaar, Diffusion of carbon in TiC_{1-y} and ZrC_{1-y}, Solid State Ion. 32-33 (1989) 824–832.
[35] W. Sun, H. Ehteshami, P.R.C. Kent, P.A. Korzhavyi, Self-diffusion of Ti interstitial based point defects and complexes in TiC, Acta Mater. 165 (2019) 381–387.
[36] S. Sarian, Diffusion of 44Ti in TiCx, J. Appl. Phys. 40 (9) (1969) 3515–3520.
[37] D. Zhao, D. Kong, J. Huang, M. Wang, T. Yamaguchi, H. Wang, Achieving the lightweight wear-resistant TiC reinforced AlFeCrCo medium-entropy alloy coating on mg alloy via resistance seam processing, Scr. Mater. 210 (2022) 114429.
[38] S. Gao, Z. Hu, M. Duchamp, P.S.R. Krishnan, S. Tekumalla, X. Song, M. Seita, Recrystallization-based grain boundary engineering of 316L stainless steel produced via selective laser melting, Acta Mater. 200 (2020) 366–377.
[39] G.K. Meenashisundaram, M. Gupta, Synthesis and characterization of high performance low volume fraction TiC reinforced mg nanocomposites targeting biocompatible/structural applications, Mater. Sci. Eng. A 627 (2015) 306–315.
[40] H. Yu, Y. Xin, M. Wang, Q. Liu, Hall-Petch relationship in mg alloys: a review, Journal of Materials Science & Technology. 34 (2) (2018) 248–256.
[41] Z. Xiao, Y. Lei, Z. Hu, C. Chen, B. Chen, H. Zhu, Influence of rescanning parameters on selective laser melting of Ti6Al4V, J. Manuf. Process. 82 (2022) 530–542.
[42] X. Ji, J. Zhao, H. Wang, C. Luo, Sliding wear of spark plasma sintered CrFeCoNiCu high entropy alloy coatings with MoS_2 and WC additions, Int. J. Adv. Manuf. Technol. 96 (2018) 1685–1691.
[43] B.N. Sahoo, S.K. Panigrahi, Synthesis, characterization and mechanical properties of in-situ (TiC-TiB_2) reinforced magnesium matrix composite, Materials & Design. 109 (2016) 300–313.
[44] Behrouz Bagheri, Vanani, Abdollahzadeh Amin, fabrication of reinforced Al–mg composite by TiC particles via FSW: microstructure and tribology study, J. Mater. Res. Technol. 30 (2024) 6787–6801.
[45] Z.h. Zhu, K.b. Nie, P. Munroe, K.k. Deng, Y.c. Guo, J.g. Han, Synergistic effects of hybrid (SiC+TiC) nanoparticles and dynamic precipitates in the design of a high-strength magnesium matrix nanocomposite, Mater. Chem. Phys. 259 (2021).
[46] J. Subramanian, Z. Loh, S. Seetharaman, A.S. Hamouda, M. Gupta, Microstructure and mechanical properties of Mg-5Nb metal-metal composite reinforced with nano SiC ceramic particles, Metals 2 (2) (2012) 178–194.
[47] D. Shepelev, J. Klempf, M. Bamberger, A. Katsman, Grain refinement and mechanical properties enhancement of AZ91E alloy by addition of ceramic particles, J. Mater. Sci. 46 (2011) 5798–5806.
[48] J. Sun, D. Ding, W. Liu, G. Wu, H. Liu, G. Wei, H. Liu, Strength and elastic modulus enhancement in mg-Li-Al matrix composites reinforced by ex situ TiB_2 particles via stir casting, Journal of Magnesium and Alloys. 12 (9) (2024) 3574–3588.
[49] A. Meher, M.M. Mahapatra, P. Samal, P.R. Vundavilli, Study on effect of TiB_2 reinforcement on the microstructural and mechanical properties of magnesium RZ5 alloy based metal matrix composites, Journal of Magnesium and Alloys. 8 (3) (2020) 780–792.

[50] A. Erman, J. Groza, X. Li, H. Choi, G. Cao, Nanoparticle effects in cast mg-1 wt% SiC nano-composites, Mater. Sci. Eng. A 558 (2012) (2012) 39–43.
[51] M. Ra'ayatpour, M. Emamy, J. Rassizadehghani, Influence of hot extrusion on the microstructure, tensile and wear properties of Mg–5Sb–xSiC hybrid composites, Met. Mater. Int. 28 (3) (2022) 679–694.
[52] K. Ponhan, D. Weston, K. Tassenberg, Influence of SiC nanoparticle contents on microstructural evolution and mechanical behavior of AZ91D magnesium matrix composites synthesised through a combination of a master pellet feeding technique and stir casting assisted by ultrasonic vibration, Materials Today Communications. 36 (2023) 106785.